RESEARCH ARTICLE

Shear Versus Tensile Failure Mechanisms Induced by Sill Intrusions: Implications for Emplacement of Conical and Saucer-Shaped Intrusions

Ø. T. Haug[1] [ID], O. Galland[1] [ID], P. Souloumiac[2], A. Souche[1], F. Guldstrand[1] [ID], T. Schmiedel[1] [ID], and B. Maillot[2]

[1]Physics of Geological Processes, University of Oslo, Oslo, Norway, [2]Géosciences et Environnement Cergy, Université de Cergy-Pointoise, Cergy-Pointoise, France

Abstract Sills, saucer-shaped sills, and cone sheets are fundamental magma conduits in many sedimentary basins worldwide. Models of their emplacement usually approximate the host rock properties as purely elastic and consider the plastic deformation to be negligible. However, many field observations suggest that inelastic damage and shear fracturing play a significant role during sill emplacement. Here we use a rigid plasticity approach, through limit analysis modeling, to study the conditions required for inelastic deformation of sill overburdens. Our models produce distinct shear failure structures that resemble intrusive bodies, such as cone sheets and saucer-shaped sills. This suggests that shear damage greatly controls the transition from flat sill to inclined sheets. We derive an empirical scaling law of the critical overpressure required for shear failure of the sill's overburden. This scaling law allows to predict the critical sill diameter at which shear failure of the overburden occurs, which matches the diameters of natural saucer-shaped intrusions' inner sills. A quantitative comparison between our shear failure model and the established sill's tensile propagation mechanism suggests that sills initially propagate as tensile fractures, until reaching a critical diameter at which shear failure of the overburden controls the subsequent emplacement of the magma. This comparison also allows us to predict, for the first time, the conditions of emplacement of both conical intrusions, saucer-shaped intrusions, and large concordant sills. Beyond the application to sills, our study suggests that shear failure significantly controls the emplacement of igneous sheet intrusions in the Earth's brittle crust.

1. Introduction

Voluminous igneous intrusions and sand injectite complexes have been documented in many sedimentary basins worldwide (e.g., Hansen & Cartwright, 2006; Magee et al., 2016; Planke et al., 2005; Szarawarska et al., 2010). Their emplacement is a result of overpressurized fluids (magma or fluidized sediments) that forcefully create room for themselves by deforming their brittle host rock. Given the layered nature of sedimentary strata, these intrusions are dominantly flat-lying, concordant sills, but they also exhibit other shapes like cones (Duranti et al., 2002; Mourgues et al., 2012), saucer shapes (Figure 1a; Jackson et al., 2013; Planke et al., 2005; Polteau, Mazzini, et al., 2008; Szarawarska et al., 2010), transgressive sheets (Jackson et al., 2013; Planke et al., 2005), and laccoliths (de Saint-Blanquat et al., 2006; Jackson et al., 2013; Pollard & Johnson, 1973; Rodriguez Monreal et al., 2009). In addition, geophysical and geodetic data show that sills are essential components of the plumbing systems of active volcanoes, where their occurrence greatly affects magma transport and stalling prior to eruptions (Amelung et al., 2000; Magee et al., 2017; Sigmundsson et al., 2010).

Numerous field observations document the occurrence of complex deformation and damage patterns associated with the emplacement of igneous intrusions and sand injectites in sedimentary basins (Figure 1b). At local scale, that is, intrusion tip scale, significant brittle shear and/or ductile shear has been documented to accommodate the propagation of intrusion tips (e.g., Agirrezabala, 2015; Pollard, 1973; Schofield et al., 2012; Wilson et al., 2016; Spacapan et al., 2017). At larger scale, that is, at intrusion scale, some authors argue that shear failure controls, at least partly, the emplacement of magma or fluidized sediments into conical intrusions (Galland et al., 2014; Guldstrand et al., 2017; Phillips, 1974; Schmiedel, Galland, & Breitkreuz, 2017), saucer-shaped intrusions (Galland et al., 2009; Haug et al., 2017; Muirhead et al., 2016), or laccoliths (Breitkreuz et al., 2015; Corry, 1988; de Saint-Blanquat et al., 2006; Schmiedel et al., 2015; Schmiedel, Galland,
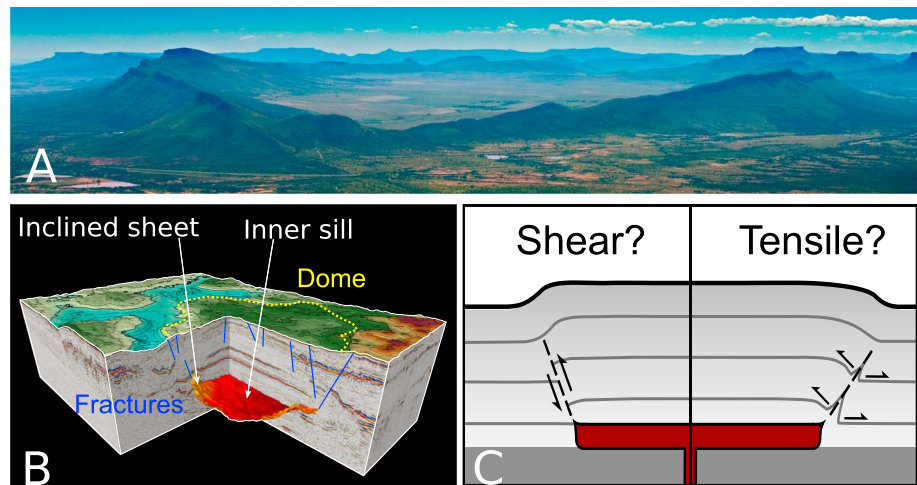
Figure 1. Saucer-shaped sills: (a) Image of the Golden Valley sill, South Africa, having roughly 10 km in diameter (Galland et al., 2009; Polteau, Mazzini, et al., 2008). (b) Seismic interpretation of the Tulipan sill, Norway, showing fractures beneath the domed paleosurface (Schmiedel, Kjoberg, et al., 2017). (c) Conceptual models of saucer-shaped sills. (right) Analytical (Goulty & Schofield, 2008; Koch et al., 1981; Pollard, 1973), numerical (Malthe-Sørenssen et al., 2004), and gelatin experiments (Kavanagh et al., 2006) models often consider elastic host rock rheology with tensile fractures at sill tips that lead to propagation. (left) Alternatively, field observation (de Saint-Blanquat et al., 2006; Wilson et al., 2016), seismic observation (Magee et al., 2017), and cohesive granular experiments (Galland et al., 2009) observe plastic damage and shear fractures related to sill emplacement.

& Breitkreuz, 2017). The resulting host rock deformation pattern and associated damage likely have important implications for fluid flow through intruded sedimentary basins (Senger et al., 2015, 2017).

These observations are evidence that inelastic deformation of the host rock plays an important role in accommodating the emplacement of intrusions. However, most models of sill emplacement only consider elastic deformation of the host rock, while the plastic component is assumed to be negligible (e.g., Fialko et al., 2001; Galland & Scheibert, 2013; Koch et al., 1981; Menand, 2008; Menand et al., 2010; Polteau, Mazzini, et al., 2008). Of those models that take the propagation of the sill into account, the propagation is assumed to occur by tensile opening at the sill tip, similar to hydrofractures (e.g., Bunger & Cruden, 2011; Goulty & Schofield, 2008; Kavanagh et al., 2006; Malthe-Sørenssen et al., 2004; Michaut, 2011), and the deformation of the overburden is assumed to occur by pure elastic bending, so that the inelastic deformation is limited to a negligible size at the tip of the sill (Rubin, 1995). Nevertheless, Scheibert et al. (2017) show that adding a small component of plastic deformation at the tips of the intrusions can significantly modify their emplacement dynamics. In addition, Haug et al. (2017) show that the emplacement of saucer-shaped intrusion's inclined sheets are likely governed by shear failure, and associated damage, of the sill overburden. The models of Scheibert et al. (2017) and Haug et al. (2017) therefore suggest that the elastic assumption of the established models of sill and laccolith emplacement is too simplistic, and this may explain why these models cannot reproduce the natural diversity of intrusion shapes (from conical, saucer-shaped, to flat concordant sills).

To date, our current understanding of how inelastic deformation governs intrusion emplacement is very limited. Consequently, it is not clear whether tensile fracturing or inelastic shear deformation of brittle host rock is the dominant mechanism accommodating intrusion emplacement (Figure 1c). Here we build on the preliminary results of Haug et al. (2017) and perform a large parameter study to derive an empirical law of the conditions for shear failure of sill overburdens. We then quantitatively compare the conditions for shear failure to those for tensile failure, and we show that shear failure might be the dominant mechanism in common geological settings. In addition, our model allows us to identify the conditions for the emplacement of cone sheets, saucer-shaped intrusions, and large, concordant sills.

2. Modeling Method
2.1. Model Concept and Setup
The aim of this study is to investigate the conditions required for plastic failure associated with sill emplacement in the Earth's brittle crust. This entails evaluating the static mechanical stability of the brittle overburden
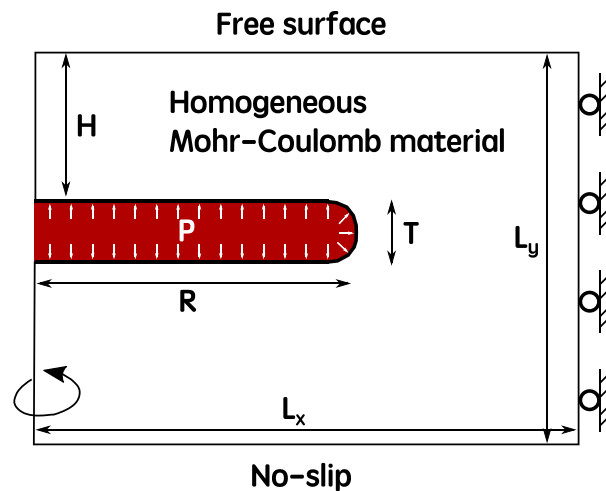
Figure 2. Sketch of setup: The system considered consists of an elongated cavity exerting a homogeneous pressure within a homogeneous and isotropic Mohr-Coulomb material. The system is in an axisymmetric setting with a free surface at the top, free slip on the right, and no slip at the bottom boundary.

of an overpressurized sill. A suitable tool for this problem is limit analysis, which is a standard engineering tool commonly applied to assess the stability of slopes, rock masses, and buildings (Sokolovski, 1960). The principle of limit analysis is to predict approximate values of loads that bring a brittle solid to an imminent state of failure (Souloumiac et al., 2009, 2010). Limit analysis is based on two theorems, the lower and upper bound theorems, also called collapse load theorems. The lower bound theorem states that failure will not occur if, for a prescribed set of loads, an equilibrium stress field can be found such that the brittle solid is everywhere below yield. Thus, the lower bound theorem can be used to find the highest prescribed load where no failure occurs. The upper bound theorem states that failure must occur if, for a prescribed set of loads, the rate of working of the external forces on the brittle solid equals or exceeds the rate of internal energy dissipation during failure (Davis & Selvadurai, 2005; Krabbenhoft et al., 2005). The upper bound theorem can therefore be used to find the lowest prescribed load that still allows failure. This implies that the actual critical load leading to failure of a brittle solid is in between the loads calculated from the lower bound and upper bound theorems. If the range between load estimates calculated from the lower and upper bound is small, the actual critical load that leads to failure is well constrained.

In this study, we apply limit analysis to constrain the critical pressure within a sill that is required to trigger failure of the brittle overburden. The model considers a sill represented by an elongated pressurized cavity of radius R, already emplaced at a depth H in a homogeneous and isotropic Mohr-Coulomb host rock of density ρ, cohesion C, and angle of friction ϕ (Figure 2); the sill thickness is set constant at 50 m. To investigate the failure conditions of the sill's overburden, we use the limit analysis software Optum G2 (Krabbenhøft & Lyamin, 2014). The entire numerical domain is 25 km wide and 8 km high. The system is solved using an adaptive grid with approximately 10,000 elements in an axisymmetric setting (see Krabbenhøft & Lyamin, 2014 for more details). We use a free surface on the upper boundary, a semi free-slip condition is applied to the right boundary (Figure 2). At the lower boundary, a no-slip condition is used. Several tests have been run using different sill tip shapes, domain sizes, and boundary conditions, which have all been documented to produce negligible effects.

Here we present results from varying geometrical parameters and host rock properties: The host rock cohesion is varied from 2.5 MPa to 100 MPa (Schellart, 2000, and references therein), the angle of internal friction is varied from 15° to 60°, and the sill's radius is varied from 100 m to 10,000 m (see also section 3, Figure 7, and Table 1). The density of the host rock is set to 2,500 kg/m^3 and the depth of emplacement is varied from 500 m to 4,000 m. For each set of parameters, the results of the calculations are (1) both the lower and upper bound solutions of the critical pressure P_c required for brittle failure of the sill's overburden and (2) the resulting distribution of energy dissipation, which we will refer to as "damage."

The assumptions of our models are the following. The mechanical effect of magma within the sill is treated as a homogeneous pressure, such that magma flow and magma density are not accounted for. Further,

Table 1
List of Parameters Used in This Study and the Range of Values

Symbol	Parameter definition	Range of values
C	Cohesion of host rock (MPa)	2.5 – 100
g	Gravitational acceleration (m/s^2)	9.81
H	Depth of emplacement of sill (m)	500 – 4,000
R	Radius of sill (m)	100 – 10,000
T	Thickness of sill (m)	50
ρ	Density of host rock (kg/m^3)	2,500
ϕ	Angle of friction of host rock	15° – 60°
$\frac{T}{R}$	Thickness-to-radius ratio of sill	0.05 – 0.5
$\frac{R}{H}$	Radius-to-depth ratio of sill	0.05 – 20.0
$\frac{C}{\rho g H}$	Cohesion-to-lithostatic stress ratio of overburden	0.05 – 2.0

the critical pressures estimated from limit analysis are calculated for complete collapse of the system, and any propagation of the damage is ignored. The limit analysis formulation considers static systems, as the aim is to investigate the conditions for failure of the overburden of a sill of a given geometry. Thus, we assume that the considered sill is emplaced, and we do not consider any host rock damage occurring during the early emplacement of the sill. This assumption implies that the earlier emplacement of the considered sill was associated with limited damage.

2.2. Dimensional Analysis and Scaling

The aim of our study is to understand how the model parameters listed in the former section and in Table 1 affect the critical pressure P_c necessary to trigger failure of the sill's overburden (Figure 2). In other words, the problem consists of finding the function f that satisfies the relation:

$$P_c = f(C, R, H, \rho, g, \phi). \tag{1}$$

where g is the gravitational acceleration. The challenge here is to find the function f that involves six variables that are likely interrelated. Instead, one can reduce the number of variable parameters by applying dimensional analysis (Barenblatt, 2003; Gibbings, 2011). The six dimensional variable parameters (and their dimensions) are as follows: the sill's radius R (m) and depth H (m), the gravitational acceleration g (m/s^2), the host rock density ρ (kg/m^3), cohesion C (Pa), and angle of friction ϕ (−). From these variables, we define a set of dimensionless variable parameters:

$$\frac{R}{H}, \qquad \frac{C}{\rho g H}, \qquad \phi. \tag{2}$$

The geometric ratio R/H expresses how wide the sill is with respect to its depth: $R/H \gg 1$ means that the sill can be considered as large and shallow, whereas $R/H \ll 1$ means that the sill is small and deep. Natural values of R/H are in between these two end member regimes (Table 1). Note that the established models of sill emplacement are based on thin plate theory, which assumes that $R/H > 5$, that is, large, shallow sills (Galland & Scheibert, 2013; Pollard & Johnson, 1973; Scaillet et al., 1995; Scheibert et al., 2017). The ratio $C/\rho g H$ expresses whether the host rock deformation is gravity dominated ($C/\rho g H \ll 1$), that is, the cohesive forces of the rock are negligible with respect to the weight, so that the material behaves as a weak material, or cohesion-dominated ($C/\rho g H \gg 1$). Natural values of $C/\rho g H \ll 1$ for sills overburden show that it is commonly gravity dominated, with the exception of shallow sills emplaced in very cohesive rocks.

When studying magma emplacement mechanics, it is more convenient to consider the critical magma overpressure, which is the effective pressure that drives propagation and emplacement (e.g., Hogan et al., 1998), instead of the absolute critical magma pressure P_c:

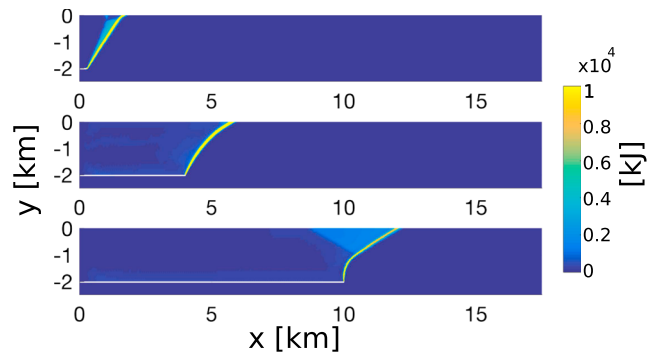$$\Delta P_c = P_c - \rho g H, \tag{3}$$

Figure 3. Cross-section maps of damage distribution from three models with varying values of R/H. (top) $R/H = 0.05$, (middle) $R/H = 2$, (bottom) $R/H = 5$. The other parameters are kept constant ($C/(\rho g H) = 0.2$, $\phi = 30°$). The horizontal white lines locate the considered sill. The color scale represents the energy dissipated by damage (in kJ), which shows a localization from the tip of the sill toward the surface.

We define a dimensionless ratio $\Delta P_c / \rho g H$, which expresses the relative value of the critical magma overpressure with respect to the confining pressure. From equations (1) and (2), the physical problem considered in our study now consists of finding the function f^* that satisfies the relation

$$\frac{\Delta P_c}{\rho g H} = f^* \left(\frac{C}{\rho g H}, \frac{R}{H}, \phi \right). \tag{4}$$

Note that we do not include in the analysis the thickness-to-radius ratio of the sill. Haug et al. (2017) show that variable values of this ratio has negligible effect on the modeling results as long as it is $\ll 1$, which is the case for most sills, given that they are sheet intrusions. In the rest of this paper, we will address the physical effects of the dimensionless ratios defined in equation (2) on both the damage distribution in the overburden and the ratio $\Delta P_c / \rho g H$, and ultimately we aim at constraining the function f^*.

3. Results

3.1. Damage Distribution in Overburden

The distribution of damage for simulations of various values of R/H, $C/(\rho g H)$, and ϕ are presented in Figures 3 and 4. In these figures, the horizontal white lines locate the considered sill, and the color distribution in the host rock represents the intensity of the energy dissipated by damage. In all simulations, the energy dissipation concentrates in a narrow zone from the sill tip toward the free surface. In the following sections, this zone of concentrated energy dissipation will be referred to as "damage zone."

Figure 3 presents the distribution of damage for different values of R/H, while keeping constant $C/(\rho g H) = 0.2$ and $\phi = 30°$. For low R/H, the damage creates an almost straight line from the sill tip to the surface (Figure 3, top), but at intermediate R/H the damage zone curves slightly (Figure 3, middle). At large values of R/H, the damage zone is strongly curved, dipping nearly vertically at the sill tip while having a gentler angle ($\approx 30°$) close to the surface (Figure 3, bottom).

The distribution of damage for changing $C/(\rho g H)$-ratios are presented in Figure 4a, where $R/H = 5$ and $\phi = 30°$. For $C/(\rho g H) = 0.2$ the damage zones resemble those in Figure 3 with damage concentrated from the sill tip all the way up to the surface (Figure 4a, left panel). Note that such features are common for all simulations with lower values of $C/(\rho g H)$. Conversely, for $C/(\rho g H) = 1$ and 2, the sharp concentrated damage zones are observed to no longer reach the surface (Figure 4a, middle and right panels). Instead, it appears to die out some distance away from the tip and a triangle of distributed damage is observed above it. We will see later that such transition occurs only in models with values of $C/(\rho g H)$ larger than a critical value C_C of about 0.4.

Figure 4b shows that the distribution of damage is significantly affected by the angle of friction ϕ. Note that the value of $C/(\rho g H) = 0.2$ in the three models displayed in Figure 4b is below the critical value C_C mentioned in the former paragraph, such that the models calculate damage across the entire sill overburden. At low angle of friction ($\phi = 15°$, i.e., that of weak shale), the damage zone appears as a steeply dipping curved line (Figure 4b, left), while it is less curved and more gently dipping for an intermediate friction angle
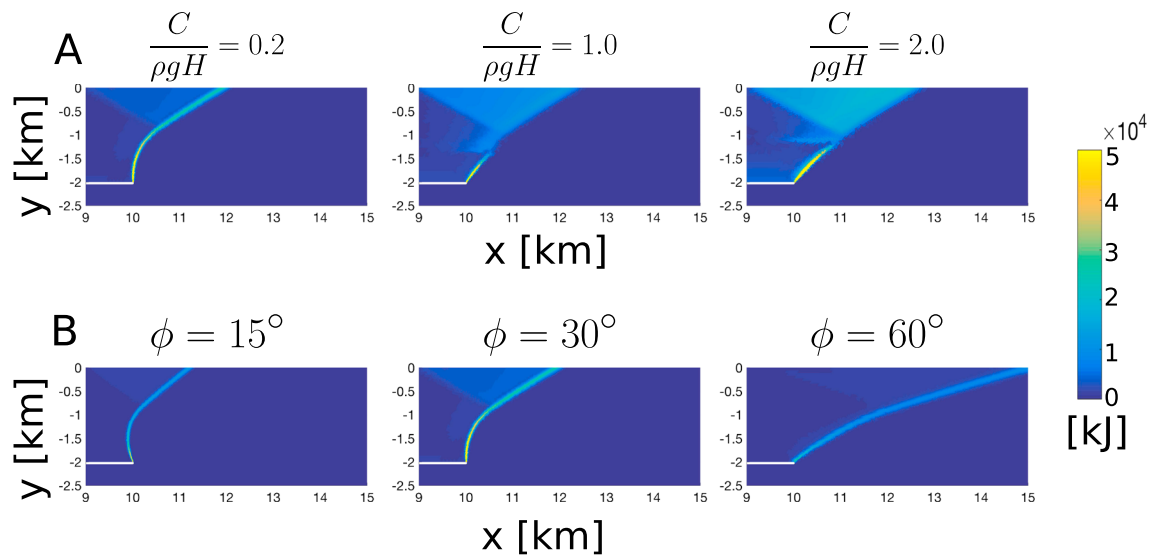
Figure 4. (a) Cross-section maps of damage distribution from three models with varying values of $C/\rho g H$. The other parameters are kept constant ($\phi = 30°$, $R/H = 5$). (b) Cross-section maps of damage distribution from three models with varying values of ϕ. The other parameters are kept constant ($C/(\rho g H) = 0.2$, $R/H = 2$). In both (a) and (b), the color scale represents the energy dissipated by damage (in kJ).

($\phi = 30°$; Figure 4b, middle). At a high angle of friction ($\phi = 60°$, i.e., that of intact granite), the damage zone is gently dipping from the sill tip toward the surface (Figure 4b, right).

We quantified the changes of the geometry of the damage zones by measuring their dip angles at the sill tip (v_{tip}) and at the free surface (v_{surf}, Figure 5a). Figure 5b displays how these angles vary with R/H for four different ratios of $C/(\rho g H)$, which are all below the critical value C_c and that makes the measurement of v_{surf} possible. Regardless of the value of $C/(\rho g H)$, the values of v_{tip} and v_{surf} collapse on the same trend. At low values of $R/H < 1$, both v_{tip} and v_{surf} exhibit roughly constant values around 60° and 50°. The difference of $(v_{tip} - v_{surf}) \approx 10°$ reflects the linear shape of the damage zones (Figure 5b). A sharp transition occurs from $R/H \approx 1$, where v_{surf} rapidly decreases with increasing R/H to a constant value of ~30°, while v_{tip} increases steadily with increasing R/H until a value of ~80° for $R/H = 5$. This sudden increase of $(v_{tip} - v_{surf})$ reflects the transition from sublinear damage zone for $R/H < 1$ to curved damage zones for $R/H > 1$ (Figure 3).

When $C/(\rho g H) > C_c \approx 0.4$, the evolutions of v_{tip} and v_{surf} with R/H are more complex (Figure 5c). At values of $R/H < 5$, the evolutions of v_{tip} and v_{surf} are similar to the cases when $C/(\rho g H) < C_c$. However, for increasing R/H, a sharp transition occurs where v_{surf} is no longer defined, and v_{tip} is observed to shift down to lower angles, before gradually increasing again with increasing R/H (Figure 5c). This new trend reflects the damage zones that do not cross the entire overburden, as described in Figure 4a. Note that the critical value of R/H between these two deformation regimes depends on the value of $C/(\rho g H)$: it decreases from $R/H = 8$ to $R/H = 5$ for increasing values of $C/(\rho g H)$ from 0.4 to 2 (Figure 5c, inset).

We also investigated the effect of the angle of internal friction (ϕ) on the morphology of the damage zone. We observe that both the angles v_{tip} and v_{surf} decrease sublinearly with increasing ϕ (Figure 5d), showing that the damage zone dips shallower with increasing ϕ, as already observed in Figure 4b. For all values of ϕ, $v_{tip} > v_{surf}$ showing that the damage zone is curved. However, $(v_{tip} - v_{surf})$ decreases with increasing ϕ (Figure 5d), showing that the damage zone becomes straighter with increasing angle of friction, as already observed in Figure 4b.

The damage patterns observed in Figures 3 and 4 can be categorized into three cases: (1) straight damage zones when $R/H < 1$, (2) curved damage zones when $R/H > 1$ and $C/(\rho g H) < C_c$, and (3) damage zones that do not reach all the way to the surface when $R/H > 5$ and $C/(\rho g H) > C_c$. Figure 6 displays the stress trajectories of the maximum (σ_1) and least (σ_3) principal stresses for each of these cases. In both Cases (1) and (2), the trajectories of σ_1 are oblique to the damage zone, with an angle systematically around 30° (Figures 6a and 6b). Given that the angle of internal friction in the models displayed in Figure 6 is $\phi = 30°$, this angular relation shows that the dominant damage is caused by shear failure. However, a clear difference is observed between
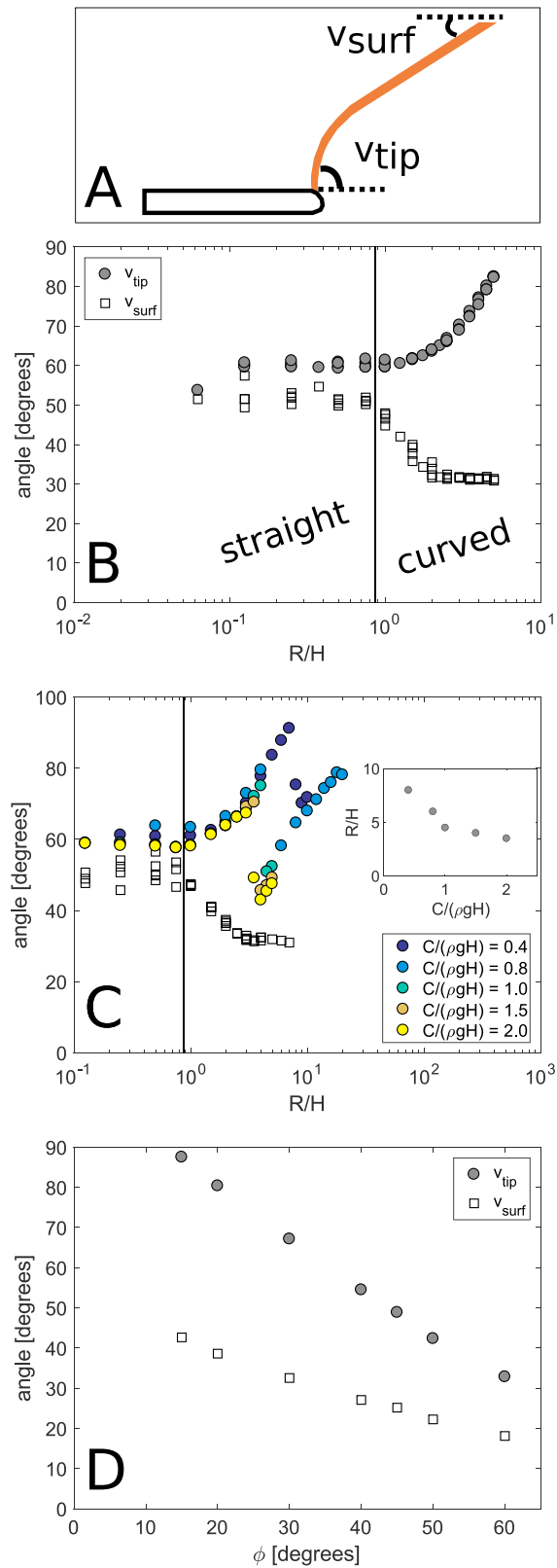
Figure 5. Geometry of damage zones. (a) Sketch showing where the angles v_{tip} and v_{surf} are measured. (b) Plot of the angle of v_{tip} (circles) and v_{surf} (squares) as a function of R/H for cases when $C/(\rho g H) < C_c$. (c) Plot of the angle of v_{tip} (circles) and v_{surf} (squares) as a function of R/H for cases when $C/(\rho g H) > C_c$ is reached. Inset shows the critical R/H value where $C/(\rho g H) \approx C_c$. (d) Plot of v_{tip} (circles) and v_{surf} (squares) as a function of ϕ.
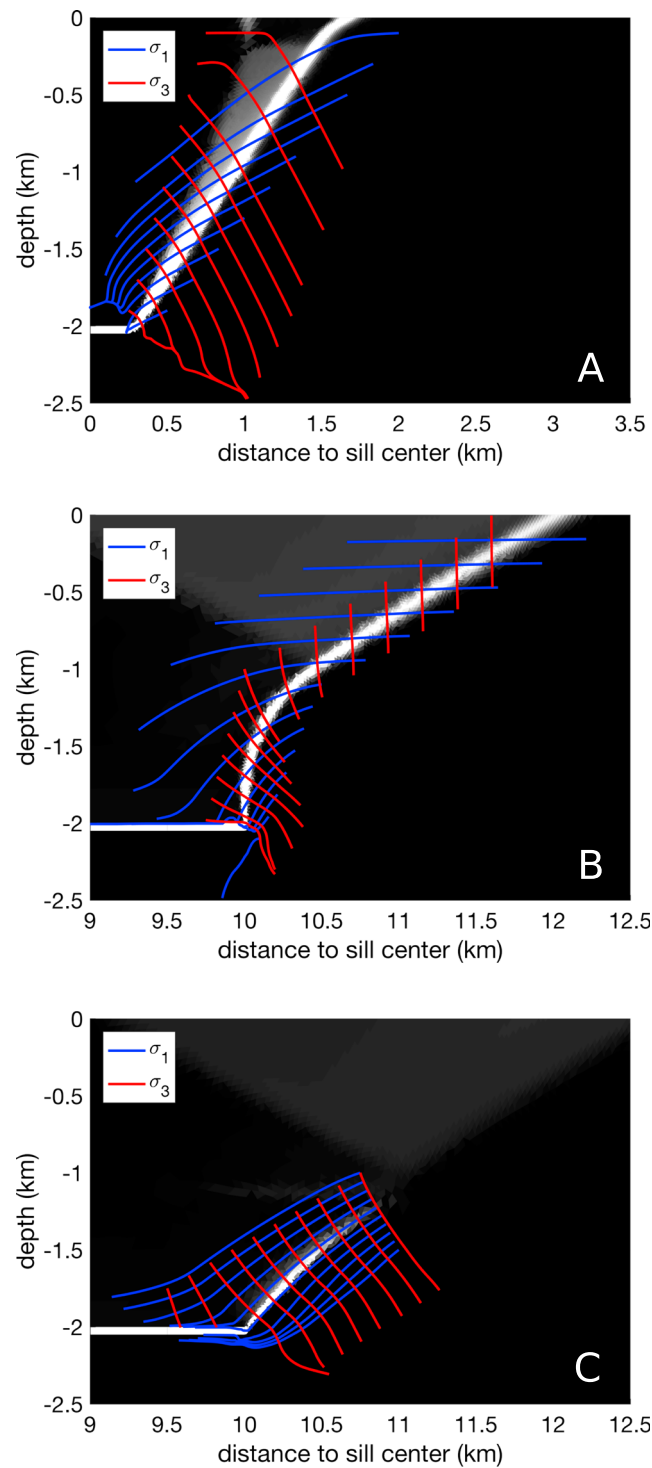
Figure 6. Stress trajectories near the damage zones. Stream lines of the principal stresses with σ_1 in blue and σ_3 in red around the damage zone. Panels (a) and (b) show the stress trajectories for cases (1) and (2), where the damage zones dominantly orients itself obliquely to the principal stresses. (c) The stress lines for case (3) where the damage zones is dominantly oriented parallel to σ_1 and orthogonally to σ_3.
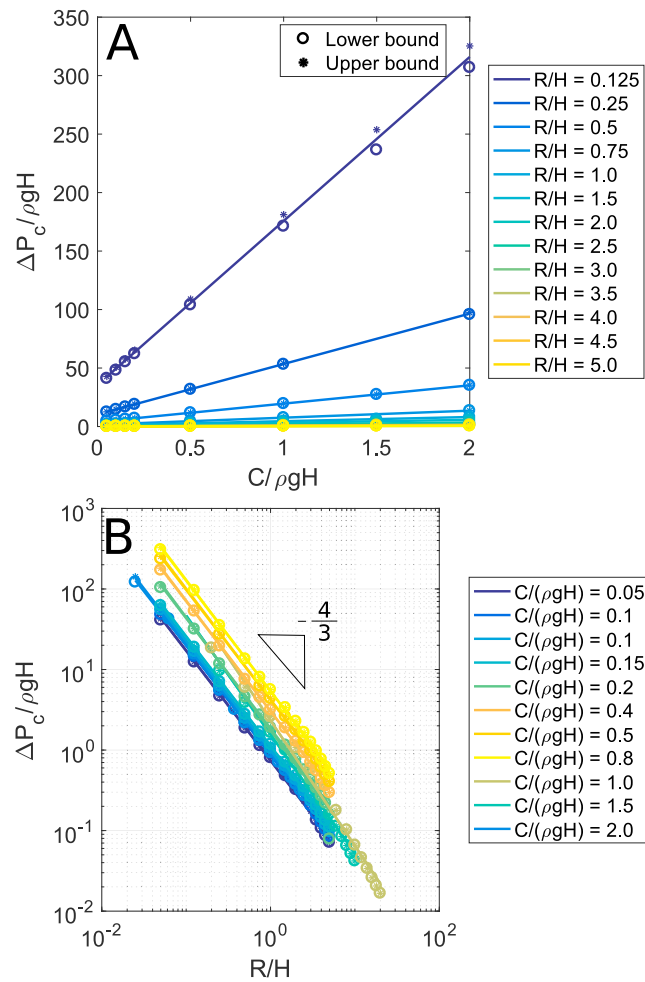
Figure 7. Failure conditions. Parameter study of $C/(\rho gH)$ (a) and R/H (b) on $\Delta P_c/(\rho gH)$. (a) The overpressure increases linearly with cohesion with a slope and intersect that depends on R/H. (b) The overpressure reduces as a power law with radius with a coefficient that varies with $C/\rho gH$, while the exponent appears to be unaltered.

these two cases and Case (3): For $C/(\rho gH) > C_c$, the damage zone is oriented dominantly parallel to σ_1 and orthogonal to σ_3 (Figure 6c), which is consistent with tensile failure. We infer from this difference that Cases (1) and (2) are dominantly caused by shear failure, whereas for Case (3) it is dominantly caused by tensile failure.

3.2. The Critical Overpressure

An important result of our models is the critical pressure ΔP_c in the sill required to trigger failure of the overburden. Here we develop the analysis based on the dimensionless parameters defined in equation (2) in order to constrain empirically the function f^* of equation (4). To achieve this, we implemented a systematic parameter study to investigate how the dimensionless critical overpressure $\Delta P_c/(\rho gH)$ varies with each governing dimensionless ratio while keeping the others constant. We foresee that there is not a simple dependence of $\Delta P_c/(\rho gH)$ with respect to ϕ; therefore, we apply a systematic procedure to test the effects of $C/(\rho gH)$ and R/H only on $\Delta P_c/(\rho gH)$. Note that the estimates of the critical overpressures calculated with the lower bound (circles) and the upper bound (squares) solutions plot almost on top of each other (Figure 7), showing that the critical overpressures are well constrained.

The overpressures required for shear failure in the sill overburden, calculated with all tested parameters (see Table 1), are presented in Figure 7; the $\Delta P_c/(\rho gH)$ ratio varies from ~0.01 to almost 350. Figure 7a shows that $\Delta P_c/(\rho gH)$ is a linear function of $C/(\rho gH)$. Both the slope of the line and its intersect with the y axis increase with increasing values of R/H. Figure 7b shows that $\Delta P_c/(\rho gH)$ is linked to R/H through a power law. The slope of the power laws with varying values of $C/(\rho gH)$ are constant, showing that the exponent of the power law is independent of $C/(\rho gH)$.

We use this systematic data set to define empirically the scaling law f^* linking the dimensionless critical overpressure $\Delta P_c/(\rho g H)$ to the dimensionless governing parameters (see equation (4)). The details of the analysis are described in the supporting information. The result of the analysis leads to the following empirical law:

$$\frac{\Delta P_c}{\rho g H} = \left(A \frac{C}{\rho g H} + B \right) \left(\frac{R}{H} \right)^{-e}. \tag{5}$$

Here A, B, and e are functions of the angle of friction ϕ only:

$$A = \alpha_1 \phi + \beta_1,$$
$$B = \alpha_2 \tan \phi,$$
$$e = \alpha_3 \log \phi + \beta_3, \tag{6}$$

and $\alpha_1 = 0.05$, $\beta_1 = 0.7$, $\alpha_2 = 1.68 \approx 5/3$, $\alpha_3 = 0.46 \approx 1/2$, and $\beta_3 = 0.69 \approx 2/3$ are fitting constants.

The values of the fitting parameters strongly control the behavior of the empirical scaling law. The function $A(\phi)$ increases sublinearly with ϕ; however, the dependence is very modest given the small value of the slope $\alpha_1 = 0.05$. Consequently, A varies between 1.7 and 3.3 within a range $20 < \phi < 50$, therefore the effect of the angle of friction on $\Delta P_c/\rho g H$ is of a factor 2 at a maximum. The exponent $-e(\phi)$ is always negative and gently varied, an average value being $-e \approx -4/3$ (supporting information; Figure 7). This value of the exponent e shows that the critical overpressure $\Delta P_c/\rho g H$ greatly decreases with increasing R/H, indicating that shear failure of the overburden is favorable for large, shallow sills.

4. Interpretation

4.1. Damage Zone Geometry

The curved damage zones ($R/H > 1$) combined with the flat preexisting sills (Figures 3 and 4) share strong resemblance to saucer-shaped intrusions (Jackson et al., 2013; Malthe-Sørenssen et al., 2004; Planke et al., 2005; Polteau, Mazzini, et al., 2008; Szarawarska et al., 2010). Haug et al. (2017) discussed the likely link between the damage zones calculated in our models and the emplacement of saucer-shaped sills' inclined sheets. These authors suggest that the damage zones induced by the overpressurized sills represent weak pathways, which control the subsequent emplacement of the magma along inclined sheets. Consequently, the inelastic deformation of the sill overburden is a precursor for saucer-shaped intrusions. The results presented here confirm these results for a wide range of emplacement depths, sill radii, and host rock properties, thus strengthening the hypothesis that the emplacement of saucer-shaped intrusions can be controlled, at least partly, by shear failure of their overburden.

Our simulations produced three distinct damage zone geometries depending on the model parameters (Figures 3 and 4): (1) relatively straight damage zones from sill tips to the surface, (2) curved damage zones from the sill tip to the surface, and (3) short damage zones rooted at the sill tips and restricted below a certain depth, above which damage is distributed. The stress trajectories presented in Figure 6 suggest that Cases (1) and (2) are caused by shear failure of the sill overburden, while Case (3) is caused by tensile failure at the sill tip.

Case (1) occurs systematically when $R/H < 1$, suggesting that if small sills manage to fail their overburden, they do so along straight shear damage zones (Figure 3, top). Such geometry are very similar to V-shaped sand injectite intrusions observed in sedimentary basins (Cartwright et al., 2008; Mourgues et al., 2012) and cone sheets observed in volcanic systems (Burchardt et al., 2011; Galland et al., 2014; Mathieu et al., 2015). Previous laboratory (Galland et al., 2014; Guldstrand et al., 2017) and theoretical (Phillips, 1974) models have suggested that shear failure plays a significant role during cone sheet formation. This is in good agreement with our results, and we infer that straight damage zones modeled in our simulations are at the origin of cone sheet emplacement. Similar features have been observed in experiments of fluid-induced deformation, leading to the formation of hydrothermal vent complexes (Nermoen et al., 2010), showing that straight shear damage zones are a fundamental response to small source of fluid overpressure, assuming the fluid overpressure is sufficient to deform the overburden.

Case (2) occurs in two distinct parameter conditions: (1) when $C/(\rho g H) < 0.4$, Case (2) occurs systematically for values of $R/H > 1$, and conversely (2) for larger values of $C/(\rho g H)$, Case (2) occurs when R/H ranges from 1 to an upper value that depends on the value of $C/(\rho g H)$ (Figure 5). The observed curved damage zones

of Case (2) match well the intrusion's curved inclined sheets observed in the field (Polteau, Ferré, et al., 2008; Polteau, Mazzini, et al., 2008), on seismic data (Szarawarska et al., 2010; Schmiedel, Kjoberg, et al., 2017), and those produced in laboratory models (Galland, 2012; Galland et al., 2009). This suggests that shear failure is likely common in nature. The transition between Cases (1) and (2) was recognized by Haug et al. (2017) in a single series of simulations. Importantly, the transition from straight to curved damage zones always occur at $R/H \sim 1$, regardless of the host rock properties. This suggests that it is a fundamental mechanical transition during shear failure of sill overburden when the sill radii become comparable to their depths of emplacement.

Case (3) occurs when $C/(\rho gH) > 0.4$ and when R/H is higher than a critical value that range between 5 and 8, depending on the value of $C/(\rho gH)$ (Figure 5c, inset). This damage morphology, as well as the transition between Cases (2) and (3), has not been described before. It is interesting to note that the transition between Cases (2) and (3) occurs for high values of R/H (5–10) and for relatively large values of $C/(\rho gH)$. This implies that most sills in nature are associated with Case (2), that is, dominant shear failure of the overburden, whereas Case (3), that is, dominant tensile failure of the overburden, is expected to occur only for large, shallow sills emplaced in competent rocks. The conditions of occurrence of Case (3) are in agreement with the models of Goulty and Schofield (2008) and Galland and Scheibert (2013), which address the formation of saucer-shaped intrusion's inclined sheets through the tensile failure of a thin, elastic overburden.

The effect of the angle of friction ϕ is quite obvious (Figure 4b). As expected, the damage zones associated with low angle of friction are steeper than those associated with high angle of friction (Figure 4b). This suggests that intrusions emplaced in low-friction shale, as commonly observed (Rodriguez Monreal et al., 2009), are likely associated with steep damage zones, whereas intrusions emplaced in high-friction consolidated sandstone are likely associated with gently dipping damage zones. Geological observations are, however, lacking to assess the relevance of the friction angle for the emplacement of real igneous intrusions. The angle of friction ϕ also affects the shape of the damage zone, given the $(v_{tip} - v_{surf})$ decreases linearly with ϕ (Figure 5d), showing that the damage zone becomes straighter with higher friction angle.

4.2. Pressure Conditions for Overburden Failure

The modeling strategy implemented in this study aims at exploring systematically the parameter space to derive the empirical scaling law of the critical overpressure required to trigger failure of the sill overburden. The linear relation between $\Delta P_c/(\rho gH)$ and $C/(\rho gH)$ (Figure 7a) indicates that the stronger the overburden, the more pressure is required to fail it. This result is quite intuitive, as well as the observed linear relationship, given that ΔP_c and C have the same dimensions. The negative exponent of the power law relation between $\Delta P_c/(\rho gH)$ and R/H (Figure 7b) shows that the larger the sill, the less pressure is required to fail the overburden. This result suggests that large sills offer favorable conditions for shear failure of their overburden.

The scaling law of equation (5) indicates that the effects of the friction angle ϕ on $\Delta P_c/(\rho gH)$ are more complex than the effects of $C/(\rho gH)$ and R/H. The main effect is related to the exponent e of our empirical scaling law. Even if the value of $-e$ varies slightly from -1.2 and -1.5 for friction angles between 15° and 60°, such change affects the behavior of the power law dependence of $\Delta P_c/(\rho gH)$ on R/H of equation (5). The value of the exponent $-e$ for a high friction angle is lower ($-e = -1.5$) than for a low friction angle ($-e = -1.2$). This implies that $\Delta P_c/(\rho gH)$ decreases faster with respect to R/H for higher friction angles, which would result in lines of steeper slopes in Figure 7.

The overpressures ΔP_c required for shear failure of sill overburdens calculated from our simulations range from 0.01 to almost 350 times the lithostatic stress, depending on R/H and $C/(\rho gH)$ (Figure 7). The highest values of $\Delta P_c/(\rho gH)$ are calculated for the lowest values of R/H and the highest values of $C/(\rho gH)$. However, it is clear that the upper range of our results is not geologically realistic. In nature, the estimated overpressures in sills range between 1 MPa to a few tens of MPa (Rubin, 1995). Assuming sill emplacement depths between 500 m and 4,000 m, this would mean that the $\Delta P_c/(\rho gH)$ ratio in nature range from 0.01 to 1.6. This condition implies that very small sills (i.e., $R/H < 0.3$) cannot trigger overburden failure and that small sills (i.e., $0.3 < R/H < 1$) can lead to failure of their overburden only when $C/(\rho gH) < 0.1$ (Figure 7b), that is, when they are emplaced in weak host rock. Conversely, our results show that larger sills are associated with more favorable overpressure conditions for failure of their overburden: for intermediate sills ($1 < R/H < 2$), the condition $\Delta P_c/(\rho gH) < 1$ is fulfilled for a wide range of $C/(\rho gH)$ ratios, while for even larger sills ($R/H > 2$), all tested scenarios fulfill the condition $\Delta P_c/(\rho gH) < 1$ (Figure 7). This implies that the curved damage zones, that is, large R/H (Figure 3, bottom), are more likely to occur in nature than the straight damage zones.
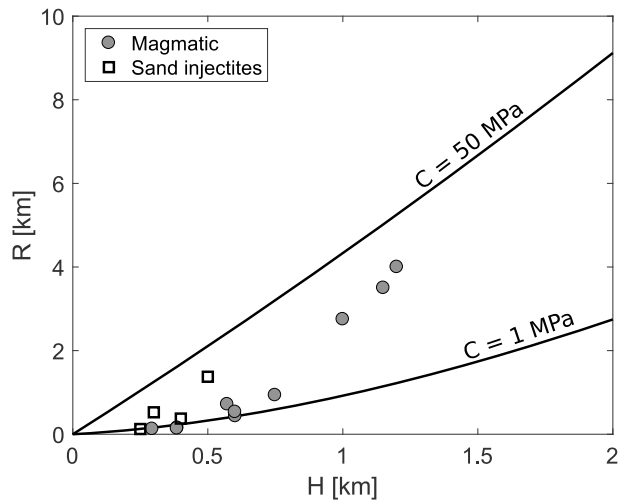
Figure 8. Radius versus depth of emplacement. The predicted radius of sills compared to their depth from equation (7) by assuming that $\Delta P_c = 20$ MPa and $C = 50$ MPa (upper line) and $C = 1$ MPa (bottom line). The gray circles and open squares represent data from nature (given in Table 1 in Polteau, Mazzini, et al., 2008).

5. Discussion

5.1. Geological Testing of Modeling Results

In the former sections, we discussed qualitatively the relevance of our model results. The aim of this section is now to test quantitatively the geological relevance of the empirical scaling law of equation (5). To do so, we will test whether our scaling law can reproduce geological trends. For example, in nature, we observe a relationship between the diameter of saucer-shaped intrusions and their depth of emplacement (Polteau, Mazzini, et al., 2008). Solving equation (5) with respect to R gives the radius of a sill at failure as a function of the depth of emplacement:

$$R = H \left(\frac{AC + B\rho gH}{\Delta P_c} \right)^{1/e} \tag{7}$$

This equation shows that R is expected to increase with H and to decrease with ΔP_c, in agreement with geological data and existing modeling results (Galland & Scheibert, 2013; Goulty & Schofield, 2008; Malthe-Sørenssen et al., 2004). It also shows a nonlinear relationship between R and H, which takes the form of a power law of exponent larger than 1. This result differs from the linear relationships derived by Goulty and Schofield (2008) and Galland and Scheibert (2013). Such nonlinear behavior has been highlighted by Malthe-Sørenssen et al. (2004), who found a relation $R \propto H^\alpha$, where the exponent $\alpha < 1$. This means that Malthe-Sørenssen et al. (2004) predicts a concave relationship between R and H, while we predict a convex relationship.

Now we will try to apply the empirical scaling law of equation (5) with typical geological values to calculate the expected inner sill diameters. We assume typical value of $\Delta P_c = 20$ MPa, and we consider a case with a competent overburden ($C = 50$ MPa) and a case with a weak overburden ($C = 1$ MPa). We consider a typical value of density ($\rho = 2,500$ kg/m^3) and angle of friction ($\phi = 30°$) of sedimentary rocks. Figure 8 displays the calculated sill radius expected to trigger overburden failure with respect to the emplacement depth for the competent (upper curve) and weak (lower curve) overburden rocks. We also display the geological values of R and H of inner sills from the literature (Polteau, Mazzini, et al., 2008), that is, the intrusion diameter at the sill-to-inclined sheet transitions. The purpose of this comparison is not to perfectly predict each individual data point from nature, as this would require much more specific information (e.g., ΔP_C and C) for each case than what is accessible. Rather, the purpose is to see whether the empirical scaling law can predict correctly the range of values seen in nature. Figure 8 shows that the geological data plot between the predictions of our model. The good match between the natural data set and our model predictions supports the geological relevance of our model. Thus, this result strengthens our hypothesis that the transition from flat inner sill to inclined sheet in saucer-shaped intrusions is triggered by the onset of shear failure of the sill's overburden.

A limitation of the limit analysis modeling approach is that it accounts for the complete failure of the sill's overburden, but not for the propagation of damage as a result of sill inflation. However, the very small difference between the lower and the upper bond estimates of the critical overpressure shows that when failure initiates, it requires very small overpressure increment to fail entirely the sill's overburden. In other words, our results suggest that as soon as the sill's overburden starts failing, it is unstable and easily fails entirely. Therefore, pressure estimates given by the scaling law of equation (5) for the full failure of the sill's overburden is a good proxy for the initiation of failure.

Note that the scaling law of equation (5) is derived empirically but is not derived from a mathematical theory of the plastic deformation related to pressurized sills within a brittle host. This approach is physically relevant, because the dimensional analysis predicted the dependency of the critical pressure on the other physical parameters of the model. This is a well-established procedure in the physics community to constrain quantitatively the physical laws of observed phenomena that are not described by a known theoretical law (Barenblatt, 2003; Gibbings, 2011). Even if our model does not include all the complexity of geological systems (e.g., viscous flow of the magma and heterogeneities of the host rock), the first-order match between our results and geological observations (Figure 8) strongly suggests that our model is physically and geologically relevant.

5.2. Reconciling the Shear Versus Tensile Propagation Models

Our model properly predicts the conditions for shear failure of the overburden of an overpressurized sill. However, the disadvantage of our model is that it assumes that the sill is already emplaced and ignores the former stage of the sill emplacement. Sills are conventionally thought to propagate as hydrofractures, that is, propagating by tensile opening fractures at its tip (e.g., Bunger & Cruden, 2011; Galland & Scheibert, 2013; Michaut, 2011; Rubin, 1995; Scheibert et al., 2017). The aim of this section is to discuss how our model of shear damage-controlled emplacement of inclined sheets is compatible with the established tensile hydrofracture propagation of sills. We propose to test the following hypothesis: sills initially propagate as tensile hydrofractures until they reach a critical radius, such that they trigger shear failure of their overburden, leading to the emplacement of inclined sheets.

To test the relevance of this hypothesis, we compare the overpressure conditions required for shear failure of the sill overburden [our model, equation (5)] to those required for tensile fracturing propagation at the sill's tip. To achieve this, we consider the model of Zhang et al. (2002), which considers an asymptotic solution to the problem of a fluid-filled fracture that propagates in an elastic medium close to the surface, that is, relevant for shallow sills. We consider here the so-called "toughness-dominated" regime, where the dynamics of the physical system are dominated by the strength of the host rock, such that the viscosity of the fluid is negligible. This model predicts that a sill propagates if the critical overpressure ΔP_c fulfills the equation:

$$\Delta P_c^I = \left(\frac{K'^6}{E'^6 V} \right)^{1/5} E' \Pi_{k0} \tag{8}$$

where ΔP_c^I describes the critical overpressure required for continued mode I fractures at the sill tip, Π_{k0} is a 10th order polynomial of R/H, V is the volume of the sill, $K' = 4\sqrt{2/\pi} K_{Ic}$ where K_{Ic} is the fracture toughness, and $E' = E/(1 - \nu^2)$ where E and ν are the Young's modulus and the Poisson ratio of the host rock, respectively.

Figure 9a displays the dimensionless critical overpressures required for (1) tensile propagation of the sill tip ($\Delta P_c^I/(\rho g H)$) from the model of Zhang et al. (2002) [red curve in Figure 9a, equation (8)] and (2) shear failure of sill overburden ($\Delta P_c/(\rho g H)$) from our model [black curve in Figure 9a, equation (5)], with respect to R/H. In the calculations displayed in Figure 9a, we consider that the sill depth $H = 1,000$ m. The mechanical parameters used in our models are cohesion of $C = 10$ MPa and friction angle of $\phi = 30°$. The mechanical parameters of the model of Zhang et al. (2002) are Young's modulus of $E = 1$ GPa and a fracture toughness of $K_{Ic} = 800$ MPa (Bunger & Cruden, 2011). We assume a sill thickness of 50 m in our model, and we estimate the sill volume $V \approx 50\pi R^2$ m³ to be used in equation (8). Figure 9a shows that for values of $R/H < 3$, the critical overpressure $\Delta P_c^I/(\rho g H)$ (gray curve) is lower than the critical overpressure $\Delta P_c/(\rho g H)$ (black straight line). This means that under these mechanical conditions, a small sill will preferably propagate as a tensile hydrofracture. In this scenario, as the sill keeps propagating, the ratio R/H increases, and the critical overpressure for shear failure $\Delta P_c/(\rho g H)$ becomes equal to the critical overpressure for tensile propagation $\Delta P_c^I/(\rho g H)$ at a critical value of $R/H > 7$ (red circle in Figure 9a). This means that there is a critical value of R/H, beyond which shear failure of the sill overburden is more favorable than tensile hydrofracture propagation. The comparison between these two model equations therefore suggests that small sills initially grow laterally as tensile hydrofractures, until they reach a critical value of R/H, where shear failure of the sill's overburden occurs, controlling the emplacement of inclined sheets. In other words, at given mechanical properties, there is a critical value of R/H that controls the tensile-to-shear failure transition. We infer that this transition controls the horizontal sill-to-inclined sheet transition.

We investigated systematically the effects of the model parameters on the critical value of R/H controlling the horizontal sill-to-inclined sheet transition. Figure 9b shows that high values of K_{Ic} lead to critical $R/H \approx 1$, which increases with decreasing K_{Ic}. Ultimately, for values $K_{Ic} < 10^9$ Pa/m$^{1/2}$, the curves from our model and the model of Zhang et al. (2002) do not cross, showing that no shear failure of the sill overburden is expected, that is, the sills remain flat and concordant when the overburden is weakly resistant to tensile failure. Figure 9c shows that the crossing between the curves from our model and the model of Zhang et al. (2002) occurs for values of $E < 10^9$ Pa only. We note also that when the crossing occurs, the critical value of R/H decreases with decreasing E. These results show that the crossing between the two curves is impeded by stiff overburden. Finally, Figure 9d shows that the crossing between the curves from our model and the model of Zhang et al. (2002) occurs for values of $C < 10^7$ Pa only. When the crossing occurs, the critical value of R/H decreases with decreasing C. These results show that the tensile-to-shear failure transition is impeded by overburden of high cohesion.
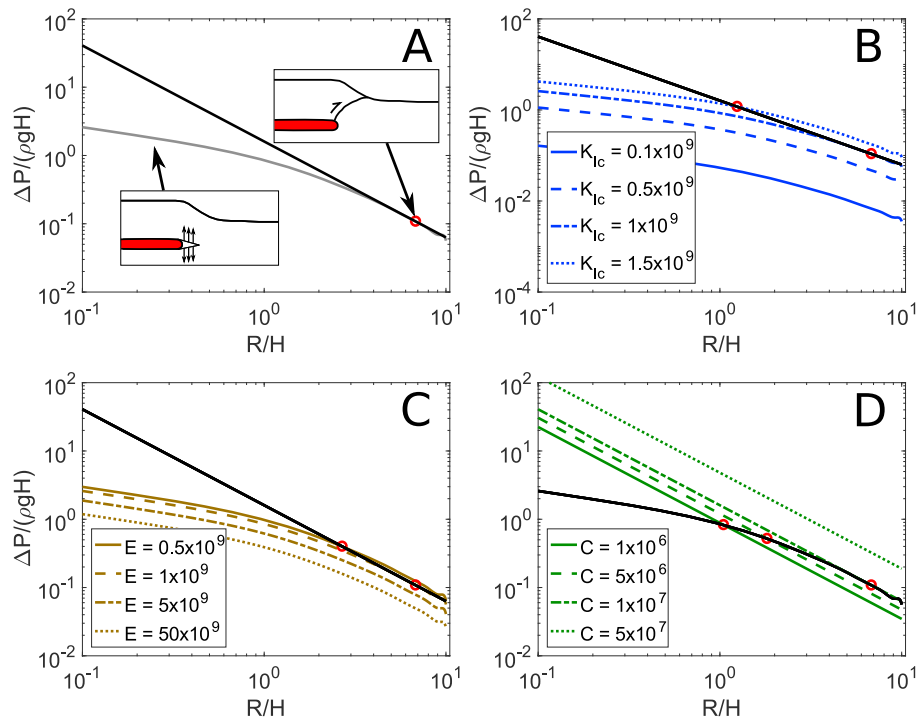
Figure 9. Transition from lateral propagation to shear failure. (a) Comparison between an asymptotic solution for pressure required for lateral propagation of a sill within an elastic medium (gray line, Zhang et al., 2002) and the scaling law proposed here (equation (5); black line). Comparison between the two models for the following: (b) Varying fracture toughness (K_{Ic}, blue lines) while keeping the condition for shear failure condition constant (black line). (c) Varying the Young's modulus (brown lines) while keeping the condition for shear failure condition constant (black line). (d) Varying the cohesion (green lines) while keeping the condition for lateral propagation constant (black line). The red circles locate the intersect between the two curves.

The results of Figure 9 show that the tensile-to-shear failure transition does not occur systematically. We therefore performed a systematic parameter study to explore under which mechanical condition this failure occurs, and at which R/H and $\Delta P_c/(\rho gH)$ values (Figure 10). Here we consider a range of fracture toughnesses (50 MPa $\leq K_{Ic} \leq$ 1,500 MPa (Bunger & Cruden, 2011; Cruden et al., 2017)), Young's moduli (0.1 GPa $\leq E \leq$ 5 GPa), and cohesions (1 MPa $\leq C \leq$ 50 MPa) (Schellart, 2000).

Figure 10a shows all the overpressures for all R/H ratios calculated in gray and where an intersect occurs in yellow (for $R/H < 1$, i.e., straight shear damage zones) and red ($R/H > 1$, i.e., curved shear damage zones). This shows that for a substantial part of the parameter space, both straight damage zones (inferred V-shaped intrusions) and curved damage zones (inferred saucer-shaped sills) are expected.

Figures 10b and 10c displays the mechanical conditions that lead to tensile-to-shear failure transition (colored domains) and those that do not lead to tensile-to-shear failure transition (gray domains). This map corroborates the results of Figure 9 and highlights that a sharp transition exists between the domain with a tensile-to-shear failure transition and the domain without. It is interesting to note that the values of R/H and $\Delta P_c/(\rho gH)$ are the highest and lowest, respectively, close to the transition. Consequently, for certain conditions, whether the shear failure occurs or not is rather precarious. Take, for example, the case of magma intruding into a sedimentary basin. The presence of this sharp transition suggests that if the mechanical conditions of a basin intruded by igneous sills are close to this transition, some sills can reach the conditions for a tensile-to-shear failure transition and develop saucer shape, whereas others will not reach the conditions for tensile-to-shear failure transition and remain concordant. Such a result explains, at least qualitatively, why volcanic basins exhibit both saucer-shaped intrusions and large concordant sills (Jackson et al., 2013; Magee et al., 2016; Planke et al., 2005; Schmiedel, Galland, & Breitkreuz, 2017; Svensen et al., 2012).
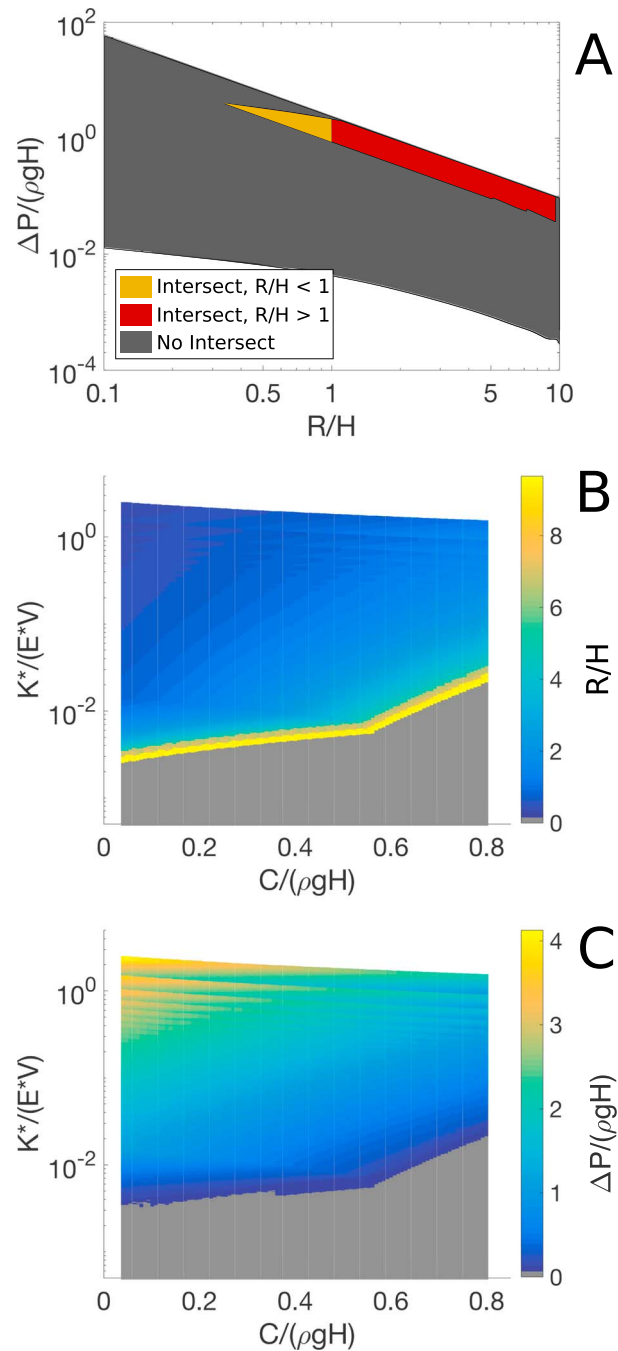
Figure 10. Phase diagrams. (a) Phase diagram showing in gray all $\Delta P_c/(\rho gH)$ values calculated over the entire parameter space tested and in red and yellow the domain of parameter space where an intersect between the equations (5) and (8) occurs. The red area displays where curved damage zones occur and in yellow where straight damage zones occur. (b) Phase diagram showing which mechanical host rock properties yield an intersection between equations (5) and 8. The colors represent the R/H ratios for the intersection and in gray the part of the parameter space where no intersect occurs. (c) Similar to (b) but with the color representing the value of $\Delta P_c/(\rho gH)$ at the intersect between equations (5) and (8).
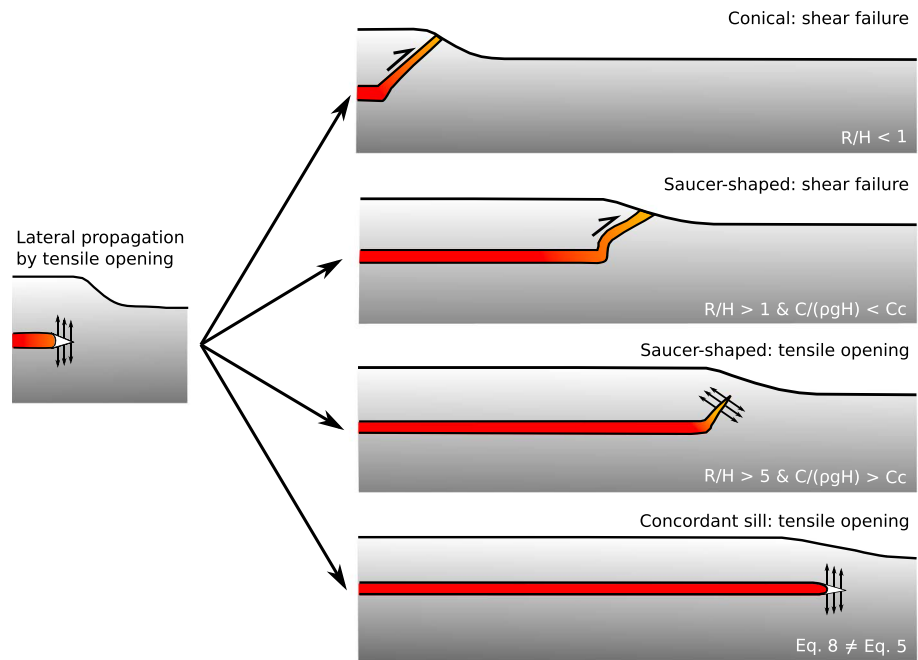
Figure 11. Illustration of proposed scenarios for cone sheet and saucer-shaped sill formation. Once a sill is formed, it propagates laterally by tensile opening at its tip. At a certain radius, shear failure of the overburden that becomes favored over tensile opening at the tip created a damage zone similar to that presented in Figures 3 and 4. The magma predominantly follows the weakness created by the damage. Should shear failure occur for $R/H < 1$, a cone sheet will be produced, and should $R/H > 1$ a saucer-shaped sill will be produced. If $R/H > 1$ and $C/(\rho g H) < C_c$, the saucer-shaped sill is caused by through-going shear failure of the sill overburden, but if $C/(\rho g H) > C_c$, it would be caused by tensile failure in the overburden.

To summarize, the results from our models highlight the following emplacement of sills, saucer-shaped sills, and V-shaped intrusions (Figure 11). Once a sill is formed, it propagates laterally by tensile opening at the sill tip, until reaching a critical value of R/H. The subsequent propagation can occur in four distinct scenarios.

1. If the sill overpressure is high and/or the overburden is weak, the sill can trigger failure of its overburden when $R/H < 1$, and shear failure occurs along straight damage zone, controlling the emplacement of V-shaped intrusions.

2. If the sill emplaces not too close to the surface and within host rock of typical cohesion values, that is, $C/(\rho g H) < 0.4$, the sill can trigger failure of its overburden when $R/H > 1$, and shear failure occurs along curved damage zones, controlling the emplacement of saucer-shaped sills.

3. Conversely, if sills are shallow and emplaced in high-cohesion rock, that is, $C/(\rho g H) > 0.4$, the sill can trigger failure of its overburden for a value of R/H larger than a critical value between 5 and 10 (depending on the value of $C/(\rho g H)$; see Figure 5c), tensile failure occurs at the tip, rather than shear failure.

4. Finally, if the elastic stiffness and resistance to tensile failure of the overburden are high and/or if its cohesion is high, the sill is expected to keep propagating horizontally (Figure 10), leading to a large, concordant sill as observed in numerous sedimentary basins.

5.3. Implications of Our Model to Magma Emplacement in the Earth's Brittle Crust

The results of our limit analysis modeling highlights that inelastic deformation of the sill's overburden can develop along shear planes all the way from the intrusion tip to the surface. The consistent similarity between the modeled damage zone and the saucer-shaped intrusions' inclined sheets suggests that the emplacement of inclined sheets are to a large degree controlled by shear failure induced by the inflating sill. In addition, the sill radius calculated with our empirical scaling law of equation (5) reproduces well the radius of inner sills observed in nature. Thus, these results suggest that the inner sill-to-inclined sheet transition is controlled by the onset of shear failure of the sill overburden, indicating that shear failure is a governing factor controlling the emplacement of inclined sheets. These results confirm the preliminary results of Haug et al. (2017). The geological relevance of our model is supported by the fact that it explains and assesses the mechanical

conditions of (1) the occurrence of V-shaped intrusions, (2) the formation of curved inclined sheets of saucer-shaped sills, and (3) the occurrence of large concordant sills (Figure 11).

Shear damage associated with the emplacement of sills and laccoliths has been observed in the field, both in sedimentary settings (e.g., de Saint-Blanquat et al., 2006; Pollard, 1973; Spacapan et al., 2017; Wilson et al., 2016) and in basaltic volcanoes (e.g., Berthod et al., 2016; Got et al., 2013). In addition, laboratory models of sill emplacement in the Coulomb brittle crust strongly suggest that plastic shear damage is likely controlling the emplacement of magma (Galland, 2012; Galland et al., 2009; Galland et al., 2014; Montanari et al., 2017; Guldstrand et al., 2017; Schmiedel, Galland, & Breitkreuz, 2017). However, most models of sills and laccolith emplacement assume that plastic failure is restricted to small process zones at the close vicinity of sill's tips and can be neglected (e.g., Bunger & Cruden, 2011; Cruden et al., 2017; Kavanagh et al., 2015; Michaut, 2011; Rivalta et al., 2013; Rubin, 1993; Thorey & Michaut, 2016); this assumption is the main foundation for the majority of the state-of-the-art mechanical models of sheet intrusion emplacement, which account for purely elastic host rock deformation. This assumption is in disagreement with the results of Scheibert et al. (2017), which show that even if plastic deformation is restricted to a very small domain at intrusion's tips, it can have nonnegligible effects on the dynamics of intrusion propagation. In addition, our models show that plastic failure is likely not restricted to domains of negligible size but might extend across large parts of the mechanical systems. This implies that the effects of plastic shear failure should not be neglected in models of sills and saucer-shaped sills and that the brittle Coulomb properties of the host rock should be accounted in these models.

Our results highlight the relevance of plastic shear deformation on the emplacement of saucer-shaped intrusions. However, our results suggest that such a mechanism is also likely at work during the emplacement of other types of intrusions in other volcanic settings. Numerous geological, geophysical, and laboratory observations corroborate this hypothesis. Spacapan et al. (2017) show how shear failure dominantly accommodates the propagation of magmatic fingers in shale-dominated sedimentary host rock (see also Pollard, 1973, and references therein). Okada et al. (1981) found that during magmatic intrusion at Usu volcano (Japan), seismicity concentrated along circular faults, suggesting extensive reverse shear failure above the intrusion. Detailed focal mechanism analysis of the seismicity associated with dike emplacement in Iceland (White et al., 2011), including the 2014 Holuhraun diking episode (Bárðarbunga volcano, Ágústsdóttir et al., 2016), show that the dominant failure mode was shear, the slip direction being parallel to the main propagation direction of the dikes. This relation between dike propagation and shear failure is in good agreement with the laboratory models of Abdelmalak et al. (2012), which show how propagating dike tips trigger conjugate shear damage, like an indenter. In addition, Eibl et al. (2017) documented that seismicity preceded the intrusion of magma along the Holuhraun dike, suggesting that damage was precursors to magma flow, in good agreement with the mechanism we propose for the emplacement of saucer-shaped intrusions. Finally, the physical analysis of the time evolution of seismicity and deformation of volcanic edifices in active volcanic systems have highlighted that most geophysical observables can be explained by diffuse to localized damage associated with inflation of magma bodies (e.g., Carrier et al., 2015; Got et al., 2017; Lengliné et al., 2008; Schmid et al., 2012). These studies strongly suggest that damage precedes magma flow, in good agreement with the conclusions of our study. Our study and the numerous evidence of plastic shear damage associated with magma emplacement show that the brittle Coulomb properties of the Earth's crust play a major role during magma emplacement and propagation, in contrast with the assumptions of the established models of sheet intrusion propagation as tensile fracture in a linearly elastic host rock.

6. Conclusions

This study reports the results of limit analysis numerical models to address the conditions for shear failure of the overburden of sills emplaced in the Earth's brittle crust. We performed a large parameter study to investigate the damage patterns associated with failure, and the critical overpressure in the sill necessary to trigger shear failure of the overburden. Our study shows that

1. The damage patterns exhibit three distinct geometries depending on the model parameters (Figures 3 and 4): Case (1) relatively straight damage zones from sill tips to the surface, Case (2) curved damage zones from the sill tip to the surface, and Case (3) short damage zones, also rooted at the sill tips but restricted below a certain depth, above which damage is distributed.

2. Straight damage of Case (1) occurs when $R/H < 1$, that is, when sill's radius is smaller than the sill's depth. Such failure mechanism is expected to occur when the magma overpressure is high and/or if the overburden is weak. This straight morphology strongly resembles V-shaped or cone sheet intrusions

3. Curved damage of Case (2) strongly resembles saucer-shaped intrusion's inclined sheets. Our models show that this failure mechanism is favorable in most geological conditions. Conversely, the damage of Case (3) occurs only for shallow sills emplaced in high-cohesion rocks.

4. The straight damage of Case (1) and the curved damage of Case (2) dominantly accommodate shear failure, whereas the damage of Case (3) dominantly accommodates tensile failure.

5. These damage patterns mimic typical intrusion morphologies (cone sheets, inclined sheets), suggesting that damage associated with shear failure is a first-order mechanical precursor for magma emplacement in the brittle crust.

6. The overpressure required to trigger shear failure follows predictable trends for variable R/H, $C/(\rho g H)$ and ϕ, which we describe in the form of an empirical scaling law [equation (5)]. This scaling law provides accurate predictions when compared to geological data (Figure 8).

7. We integrate our shear failure model with an established tensile hydrofracture propagation model, and we mapped the mechanical conditions that are favorable for shear failure or tensile failure. This analysis suggests that sills initially propagate laterally by tensile opening at the sill tip, until reaching a critical value of R/H and triggering failure of the overburden, which controls the subsequent emplacement of the magma.

8. This integration provides, for the first time, the physical conditions for the formation of V-shaped intrusions, saucer-shaped intrusions, and large concordant sills.

Our study shows that the brittle Coulomb properties of the Earth's crust can play a major role during magma emplacement and propagation.

References

Abdelmalak, M. M., Mourgues, R., Galland, O., & Bureau, D. (2012). Fracture mode analysis and related surface deformation during dyke intrusion: Results from 2D experimental modelling. *Earth and Planetary Science Letters*, *359-360*, 93–105. https://doi.org/10.1016/j.epsl.2012.10.008

Agirrezabala, L. (2015). Syndepositional forced folding and related fluid plumbing above a magmatic laccolith: Insights from outcrop (Lower Cretaceous, Basque-Cantabrian Basin, western Pyrenees). *Geological Society of America Bulletin*, *127*, 982–1000. https://doi.org/10.1130/b31192.1

Ágústsdóttir, T., Woods, J., Greenfield, T., Green, R. G., White, R. S., Winder, T., et al. (2016). Strike-slip faulting during the 2014 Bárðarbunga-Holuhraun Dike intrusion, Central Iceland. *Geophysical Research Letters*, *43*, 1495–1503. https://doi.org/10.1002/2015GL067423

Amelung, F., Jonsson, S., Zebker, H., & Segall, P. (2000). Widespread uplift and "trapdoor" faulting on Galápagos volcanoes observed with radar interferometry. *Nature*, *407*(6807), 993–996. https://doi.org/10.1038/35039604

Barenblatt, G. I. (2003). *Scaling* (171 pp.). Cambridge: Cambridge University Press.

Berthod, C., Famin, V., Bascou, J., Michon, L., Ildefonse, B., & Monié, P. (2016). Evidence of sheared sills related to flank destabilization in a basaltic volcano. *Tectonophysics*, *674*, 195–209. https://doi.org/10.1016/j.tecto.2016.02.017

Breitkreuz, C., Ehling, B.-C., & Pastrik, N. (2015). The subvolcanic units of the Late Paleozoic Halle Volcanic Complex, Germany: Geometry, internal textures and emplacement mode. In C. Breitkreuz & S. Rocchi (Eds.), *Physical geology of shallow magmatic systems: Dykes, sills and laccoliths Advances in Volcanology* (pp. 295–307). Springer International Publishing. https://doi.org/10.1007/978-3-319-14084-1_2

Bunger, A. P., & Cruden, A. R. (2011). Modeling the growth of laccoliths and large mafic sills: Role of magma body forces. *Journal of Geophysical Research*, *116*, B02203. https://doi.org/10.1029/2010JB007648

Burchardt, S., Tanner, D., Troll, V., Krumbholz, M., & Gustafsson, L. (2011). Three-dimensional geometry of concentric intrusive sheet swarms in the Geitafell and the Dyrföll volcanoes, eastern Iceland. *Geochemistry, Geophysics, Geosystems*, *12*, Q0AB09. https://doi.org/10.1029/2011GC003527

Carrier, A., Got, J.-L., Peltier, A., Ferrazzini, V., Staudacher, T., Kowalski, P., & Boissier, P. (2015). A damage model for volcanic edifices: Implications for edifice strength, magma pressure, and eruptive processes. *Journal of Geophysical Research: Solid Earth*, *120*, 567–583. https://doi.org/10.1002/2014JB011485

Cartwright, J., James, D., Huuse, M., Vetel, W., & Hurst, A. (2008). The geometry and emplacement of conical sandstone intrusions. *Journal of Structural Geology*, *30*(7), 854–867. https://doi.org/10.1016/j.jsg.2008.03.012

Corry, C. E. (1988). *Laccoliths: Mechanics of emplacement and growth* (Vol. 220). *Geological Society of America Special Paper 110*.

Cruden, A., McCaffrey, K., & Bunger, A. (2017). Geometric scaling of tabular igneous intrusions: Implications for emplacement and growth. *Advances in Volcanology*, 1–14. https://doi.org/10.1007/11157

Davis, R. O., & Selvadurai, A. P. S. (2005). *Plasticity and geomechanics*. Cambridge, UK: Cambridge University Press.

de Saint-Blanquat, M., Habert, G., Horsman, E., Morgan, S. S., Tikoff, B., Launeau, P., & Gleizes, G. (2006). Mechanisms and duration of non-tectonically assisted magma emplacement in the upper crust: The Black Mesa pluton, Henry Mountains, Utah. *Tectonophysics*, *428*(1–4), 1–31. https://doi.org/10.1016/j.tecto.2006.07.014

Duranti, D., Hurst, a., Bell, C., Groves, S., & Hanson, R. (2002). Injected and remobilized Eocene sandstones from the Alba Field, UKCS: Core and wireline log characteristics. *Petroleum Geoscience*, *8*(2), 99–107. https://doi.org/10.1144/petgeo.8.2.99

Eibl, E. P. S., Bean, C. J., Vogfjörd, K. S., Ying, Y., Lokmer, I., Möllhoff, M., et al. (2017). Tremor-rich shallow dyke formation followed by silent magma flow at Barðarbunga in Iceland. *Nature Geoscience*, *10*(4), 299–304. https://doi.org/10.1038/ngeo2906

Fialko, Y., Khazan, Y., & Simons, M. (2001). Deformation due to a pressurized horizontal circular crake in an elastic half-space, with application to volcano geodesy. *Geophysical Journal International*, *146*, 181–190.

Galland, O. (2012). Experimental modelling of ground deformation associated with shallow magma intrusions. *Earth and Planetary Science Letters*, *317–318*, 145–156. https://doi.org/10.1016/j.epsl.2011.10.017

Galland, O., Burchardt, S., Hallot, E., Mourgues, R., & Bulois, C. (2014). Dynamics of dikes versus cone sheets in volcanic systems. *Journal of Geophysical Research: Solid Earth*, *119*, 5814–5829. https://doi.org/10.1002/2014JB011151.Received

Galland, O., Planke, S., Neumann, E. R., & Malthe-Sørenssen, A. (2009). Experimental modelling of shallow magma emplacement: Application to saucer-shaped intrusions. *Earth and Planetary Science Letters*, *277*(3-4), 373–383. https://doi.org/10.1016/j.epsl.2008.11.003

Galland, O., & Scheibert, J. (2013). Analytical model of surface uplift above axisymmetric flat-lying magma intrusions: Implications for sill emplacement and geodesy. *Journal of Volcanology and Geothermal Research*, *253*(0), 114–130. https://doi.org/10.1016/j.jvolgeores.2012.12.006

Gibbings, J. C. (2011). *Dimensional analysis*. New York: Springer Science & Business Media.

Got, J. L., Peltier, A., Staudacher, T., Kowalski, P., & Boissier, P. (2013). Edifice strength and magma transfer modulation at Piton de la Fournaise volcano. *Journal of Geophysical Research: Solid Earth*, *118*, 5040–5057. https://doi.org/10.1002/jgrb.50350

Got, J.-L., Carrier, A., Marsan, D., Jouanne, F., Vogfjörd, K., & Villemin, T. (2017). An analysis of the nonlinear magma-edifice coupling at Grimsvötn volcano (Iceland). *Journal of Geophysical Research: Solid Earth*, *122*, 826–843. https://doi.org/10.1002/2016JB012905

Goulty, N. R., & Schofield, N. (2008). Implications of simple flexure theory for the formation of saucer-shaped sills. *Journal of Structural Geology*, *30*(7), 812–817. https://doi.org/10.1016/j.jsg.2008.04.002

Guldstrand, F., Burchardt, S., Hallot, E., & Galland, O. (2017). Dynamics of surface deformation induced by dikes and cone sheets in a cohesive Coulomb brittle crust. *Journal of Geophysical Research: Solid Earth*, *122*, 8511–8524. https://doi.org/10.1002/2017JB014346

Hansen, D. M., & Cartwright, J. (2006). The three-dimensional geometry and growth of forced folds above saucer-shaped igneous sills. *Journal of Structural Geology*, *28*(8), 1520–1535. https://doi.org/10.1016/j.jsg.2006.04.004

Haug, Ø. T., Galland, O., Souloumiac, P., Souche, A., Guldstrand, F., & Schmiedel, T. (2017). Inelastic damage as a mechanical precursor for the emplacement of saucer-shaped intrusions. *Geology*, *45*(12), 1099–1102. https://doi.org/10.1130/G39361.1

Hogan, J. P., Price, J. D., & Gilbert, M. C. (1998). Magma traps and driving pressure: Consequences for pluton shape and emplacement in an extensional regime. *Journal of Structural Geology*, *20*(9-10), 1155–1168. tY - JOUR.

Jackson, C. A. L., Schofield, N., & Golenkov, B. (2013). Geometry and controls on the development of igneous sill-related forced folds: A 2-D seismic reflection case study from offshore southern Australia. *Bulletin of the Geological Society of America*, *125*(11-12), 1874–1890. https://doi.org/10.1130/B30833.1

Kavanagh, J. L., Boutelier, D., & Cruden, A. R. (2015). The mechanics of sill inception, propagation and growth : Experimental evidence for rapid reduction in magmatic overpressure. *Earth and Planetary Science Letters*, *421*, 117–128. https://doi.org/10.1016/j.epsl.2015.03.038

Kavanagh, J. L., Menand, T., & Sparks, R. S. J. (2006). An experimental investigation of sill formation and propagation in layered elastic media. *Earth and Planetary Science Letters*, *245*(3-4), 799–813. https://doi.org/10. 1016/j.epsl.2006.03.025

Koch, F. G., Johnson, A. M., & Pollard, D. D. (1981). Monoclinal bending of strata over laccolithic intrusions. *Tectonophysics*, *74*(3-4), 21–31. https://doi.org/10.1016/0040-1951(81)90189-X

Krabbenhøft, K., & Lyamin, A. V. (2014). Optum G2.

Krabbenhoft, K., Lyamin, A. V., Hjiaj, M., & Sloan, S. W. (2005). A new discontinuous upper bound limit analysis formulation. *International Journal for Numerical Methods in Engineering*, *63*(7), 1069–1088. https://doi.org/10.1002/nme.1314

Lengliné, O., Marsan, D., Got, J. L., Pinel, V., Ferrazzini, V., & Okubo, P. G. (2008). Seismicity and deformation induced by magma accumulation at three basaltic volcanoes. *Journal of Geophysical Research*, *113*, B12305. https://doi.org/10.1029/2008JB005937

Magee, C., Bastow, I. D., van Wyk de Vries, B., Jackson, C. A.-L., Hetherington, R., Hagos, M., & Hoggett, M. (2017). Structure and dynamics of surface uplift induced by incremental sill emplacement. *Geology*, *45*(5), 431–434. https://doi.org/10.1130/G38839.1

Magee, C., Muirhead, J. D., Karvelas, A., Holford, S. P., Jackson, C. A., Bastow, I. D., et al. (2016). Lateral magma flow in mafic sill complexes. *Geosphere*, *12*(3), 809–841. https://doi.org/10.1130/GES01256.1

Malthe-Sørenssen, A., Planke, S., Svensen, H., & Jamtveit, B. (2004). Formation of saucer-shaped sills. *Physical Geology of High-Level Magmatic Systems*, *234*, 215–227.

Mathieu, L., Burchardt, S., Troll, V., Krumbholz, M., & Delcamp, A. (2015). Geological constraints on the dynamic emplacement of cone-sheets—The Ardnamurchan cone-sheet swarm, NW Scotland. *Journal of Structural Geology*, *80*, 133–141. https://doi.org/10.1016/j.jsg.2015.08.012

Menand, T. (2008). The mechanics and dynamics of sills in layered elastic rocks and their implications for the growth of laccoliths and other igneous complexes. *Earth and Planetary Science Letters*, *267*(1-2), 93–99. https://doi.org/10.1016/j.epsl.2007.11.043

Menand, T., Daniels, K. A., & Benghiat, P. (2010). Dyke propagation and sill formation in a compressive tectonic environment. *Journal of Geophysical Research*, *115*, B08201. https://doi.org/10.1029/2009JB006791

Michaut, C. (2011). Dynamics of magmatic intrusions in the upper crust: Theory and applications to laccoliths on Earth and the Moon. *Journal of Geophysical Research*, *116*, B05205. https://doi.org/10.1029/2010JB008108

Montanari, D., Bonini, M., Corti, G., Agostini, A., & Del Ventisette, C. (2017). Forced folding above shallow magma intrusions: Insights on supercritical fluid flow from analogue modelling. *Journal of Volcanology and Geothermal Research*, *245*, 67–80. https://doi.org/10.1016/j.jvolgeores.2017.07.022

Mourgues, R., Bureau, D., Bodet, L., Gay, A., & Gressier, J. (2012). Formation of conical fractures in sedimentary basins: Experiments involving pore fluids and implications for sandstone intrusion mechanisms. *Earth and Planetary Science Letters*, *313-314*(0), 67–78. https://doi.org/10.1016/j.epsl.2011.10.029

Muirhead, J. D., Van Eaton, A. R., Re, G., White, J. D. L., & Ort, M. H. (2016). Monogenetic volcanoes fed by interconnected dikes and sills in the Hopi Buttes volcanic field, Navajo Nation, USA. *Bulletin of Volcanology*, *78*(2), 11. https://doi.org/10.1007/s00445-016-1005-8

Nermoen, A., Galland, O., Jettestuen, E., Fristad, K., Podladchikov, Y., Svensen, H., & Malthe-Sørenssen, A. (2010). Experimental and analytic modeling of piercement structures. *Journal of Geophysical Research*, *115*, B10202. https://doi.org/10.1029/2010JB007583

Okada, H., Watanabe, H., Yamashita, H., & Yokoyama, I. (1981). Seismological significance of the 1977–1978 eruptions and the magma intrusion process of Usu volcano, Hokkaido. *Journal of Volcanology and Geothermal Research*, *9*(4), 311–334. https://doi.org/10.1016/0377-0273(81)90042-1

Phillips, W. (1974). The dynamic emplacement of cone sheets. *Tectonophysics*, *24*, 69–84.

Planke, S., Rasmussen, T., Rey, S. S., & Myklebust, R. (2005). Seismic characteristics and distribution of volcanic intrusions and hydrothermal vent complexes in the Voring and More basins. In *Proceedings of 6th Petroleum Geology Conference* (pp. 833–844). London: Geological Society.

Pollard, D. D. (1973). Derivation and evaluation of a mechanical model for sheet intrusions. *Tectonophysics*, *19*(3), 233–269. https://doi.org/10.1016/0040-1951(73)90021-8

Pollard, D. D., & Johnson, A. M. (1973). Mechanics of growth of some laccolithic intrusions in the Henry mountains, Utah, II: Bending and failure of overburden layers and sill formation. *Tectonophysics*, *18*(3-4), 311–354. https://doi.org/10.1016/0040-1951(73)90051-6

Polteau, S., Ferré, E., Planke, S., Neumann, E.-R., & Chevallier, L. (2008). How are saucer-shaped sills emplaced? constraints from the Golden Valley sill, South Africa. *Journal of Geophysical Research*, *113*, B12104. https://doi.org/10.1029/2008JB005620

Polteau, S., Mazzini, A., Galland, O., Planke, S., & Malthe-Sørenssen, A. (2008). Saucer-shaped intrusions: Occurrences, emplacement and implications. *Earth and Planetary Science Letters*, *266*(1-2), 195–204. https://doi.org/10.1016/j.epsl.2007.11.015

Rivalta, E., Pascal, K., Phillips, J., & Bonaccorso, A. (2013). Explosive expansion of a slowly decompressed magma analogue: Evidence for delayed bubble nucleation. *Geochemistry, Geophysics, Geosystems*, *14*, 3067–3084. https://doi.org/10.1002/ggge.20183

Rodriguez Monreal, F., Villar, H. J., Baudino, R., Delpino, D., & Zencich, S. (2009). Modeling an atypical petroleum system: A case study of hydrocarbon generation, migration and accumulation related to igneous intrusions in the Neuquen basin, Argentina. *Marine and Petroleum Geology*, *26*(4), 590–605. https://doi.org/10.1016/j.marpetgeo. 2009.01.005

Rubin, A. M. (1993). Tensile fracture of rock at high confining pressure: Implications for dike propagation. *Journal of Geophysical Research*, *98*, 15,919–15,935. https://doi.org/10.1029/93JB01391

Rubin, A. M. (1995). Propagation of magma-filled cracks. *Annual Review of Earth and Planetary Sciences*, *23*, 287–336. https://doi.org/10.1017/CBO9781107415324.004

Scaillet, B., Pêcher, A., Pierre, R., & Champenois, M. (1995). The Gangotri granite (Gahrwal Himalaya): Laccolithic emplacement in an extending collisional belt. *Journal of Geophysical Research*, *100*(B1), 585–607.

Scheibert, J., Galland, O., & Hafver, A. (2017). Inelastic deformation during sill and laccolith emplacement: Insights from an analytic elasto-plastic model. *Journal of Geophysical Research: Solid Earth*, *122*, 923–945. https://doi.org/10.1002/2016JB013754

Schellart, W. (2000). Shear test results for cohesion and friction coefficients for different granular materials: Scaling implications for their usage in analogue modelling. *Tectonophysics*, *324*(1-2), 1–16. https://doi.org/10.1016/S0040-1951(00)00111-6

Schmid, A., Grasso, J. R., Clarke, D., Ferrazzini, V., Bachèlery, P., & Staudacher, T. (2012). Eruption forerunners from multiparameter monitoring and application for eruptions time predictability (Piton de la Fournaise). *Journal of Geophysical Research*, *117*, B11203. https://doi.org/10.1029/2012JB009167

Schmiedel, T., Breitkreuz, C., Görz, I., & Ehling, B.-C. (2015). Geometry of laccolith margins: 2D and 3D models of the Late Paleozoic Halle Volcanic Complex (Germany). *International Journal of Earth Sciences*, *104*(2), 323–333. https://doi.org/10.1007/s00531-014-1085-7

Schmiedel, T., Galland, O., & Breitkreuz, C. (2017). Dynamics of sill and laccolith emplacement in the brittle crust: Role of host rock strength and deformation mode. *Journal of Geophysical Research: Solid Earth*, *107*, 1–12. https://doi.org/10.1002/2017JB014468

Schmiedel, T., Kjoberg, S., Planke, S., Magee, C., Galland, O., Schofield, N., et al. (2017). Mechanisms of overburden deformation associated with the emplacement of the Tulipan sill, mid-Norwegian margin Tobias. *Interpretation*, *5*(3), 1–15.

Schofield, N. J., Brown, D. J., Magee, C., & Stevenson, C. T. (2012). Sill morphology and comparison of brittle and non-brittle emplacement mechanisms. *Journal of the Geological Society*, *169*(2), 127–141. https://doi.org/10.1144/0016-76492011-078

Senger, K., Buckley, S. J., Chevallier, L., Fagereng, Å., Galland, O., Kurz, T., et al. (2015). Fracturing of doleritic intrusions and associated contact zones: Insights from the Eastern Cape, South Africa. *Journal of African Earth Sciences*, *102*, 70–85.

Senger, K., Millett, J., Planke, S., Ogata, K., Eide, C., Festøy, M., et al. (2017). Effects of igneous intrusions on the petroleum system: A review. *First Break*, *35*(6), 47–56. https://doi.org/10.3997/1365-2397.2017011

Sigmundsson, F., Hreinsdottir, S., Hooper, A., Arnadottir, T., Pedersen, R., Roberts, M. J., et al. (2010). Intrusion triggering of the 2010 Eyjafjallajökull explosive eruption. *Nature*, *468*(7322), 426–430. https://doi.org/10.1038/nature09558

Sokolovski, V. V. (1960). Statics of soil media, (translated from Russian by D. H. Jones and A. N. Schofield).

Souloumiac, P., Krabbenhøft, K., Leroy, Y. M., & Maillot, B. (2010). Failure in accretionary wedges with the maximum strength theorem: Numerical algorithm and 2D validation. *Computational Geosciences*, *14*(4), 793–811. https://doi.org/10.1007/s10596-010-9184-4

Souloumiac, P., Leroy, Y. M., Maillot, B., & Krabbenhøft, K. (2009). Predicting stress distributions in fold-and-thrust belts and accretionary wedges by optimization. *Journal of Geophysical Research*, *114*, B09404. https://doi.org/10.1029/2008JB005986

Spacapan, J. B., Galland, O., Leanza, H. A., & Planke, S. (2017). Igneous sill and finger emplacement mechanism in shale-dominated formation: A field study at Cuesta del Chihuido, Neuquén Basin, Argentina. *Journal of the Geological Society*, *174*(2013), 422–433. https://doi.org/10.1144/jgs2016-056

Svensen, H., Corfu, F., Polteau, S., Hammer, y., & Planke, S. (2012). Rapid magma emplacement in the Karoo Large Igneous Province. *Earth and Planetary Science Letters*, *325-326*, 1–9. https://doi.org/10.1016/j.epsl.2012.01.015

Szarawarska, E., Huuse, M., Hurst, A., De Boer, W., Lu, L., Molyneux, S., & Rawlinson, P. (2010). Three-dimensional seismic characterisation of large-scale sandstone intrusions in the lower Palaeogene of the North Sea: Completely injected vs. in situ remobilised sandbodies. *Basin Research*, *22*(4), 517–532.

Thorey, C., & Michaut, C. (2016). Elastic-plated gravity currents with a temperature-dependent viscosity. *Journal of Fluid Mechanics*, *805*(2016), 88–117. https://doi.org/10.1017/jfm.2016.538

White, R. S., Drew, J., Martens, H. R., Key, J., Soosalu, H., & Jakobsdóttir, S. S. (2011). Dynamics of dyke intrusion in the mid-crust of Iceland. *Earth and Planetary Science Letters*, *304*(3-4), 300–312. https://doi.org/10.1016/j.epsl.2011.02.038

Wilson, P. I. R., McCaffrey, K. J. W., Wilson, R. W., Jarvis, I., & Holdsworth, R. E. (2016). Deformation structures associated with the Trachyte Mesa intrusion, Henry Mountains, Utah: Implications for sill and laccolith emplacement mechanisms. *Journal of Structural Geology*, *87*, 30–46. https://doi.org/10.1016/j.jsg.2016.04.001

Zhang, X., Jeffrey, R., & Detournay, E. (2002). Propagation of a fluid-driven penny-shaped fracture parallel to the free-surface of an elastic solid. *International Journal of Fracture*, *115*, 125–158. https://doi.org/10.1023/A: 1016345906315